Promising Oxonitridosilicate Phosphor Host Sr$_3$Si$_2$O$_4$N$_2$: Synthesis, Structure, and Luminescence Properties Activated by Eu^{2+} and Ce^{3+}/Li$^+$ for pc-LEDs

Xiao-Ming Wang,[†] Chun-Hai Wang,[‡,§] Xiao-Jun Kuang,[‖] Ru-Qiang Zou,[⊥] Ying-Xia Wang,[†] and Xi-Ping Jing[†,*]

[†]Beijing National Laboratory for Molecular Sciences, State Key Laboratory of Rare Earth Materials Chemistry and Applications, College of Chemistry and Molecular Engineering, Peking University, Beijing 100871, China

[‡]College of Physics, Peking University, Beijing, 100871, China

[§]National Key Laboratory of Shock Wave and Detonation Physics, Institute of Fluid Physics, Mianyang, 621900, China

[‖]MOE Key Laboratory of Bioinorganic and Synthetic Chemistry, State Key Laboratory of Optoelectronic Materials and Technologies, School of Chemistry and Chemical Engineering, Sun Yat-sen University, Guangzhou 510275, China

[⊥]College of Engineering, Peking University, Beijing 100871, China

ⓢ *Supporting Information*

ABSTRACT: A novel oxonitridosilicate phosphor host Sr$_3$Si$_2$O$_4$N$_2$ was synthesized in N$_2$/H$_2$ (6%) atmosphere by solid state reaction at high temperature using SrCO$_3$, SiO$_2$, and Si$_3$N$_4$ as starting materials. The crystal structure was determined by a Rietveld analysis on powder X-ray and neutron diffraction data. Sr$_3$Si$_2$O$_4$N$_2$ crystallizes in cubic symmetry with space group $Pa\overline{3}$, $Z = 24$, and cell parameter $a = 15.6593(1)$ Å. The structure of Sr$_3$Si$_2$O$_4$N$_2$ is constructed by isolated and highly corrugated 12 rings which are composed of 12 vertex-sharing [SiO$_2$N$_2$] tetrahedra with bridging N and terminal O to form three-dimensional tunnels to accommodate the Sr^{2+} ions. The calculated band structure shows that Sr$_3$Si$_2$O$_4$N$_2$ is an indirect semiconductor with a band gap ≈ 2.84 eV, which is close to the experimental value ≈ 2.71 eV from linear extrapolation of the diffuse reflection spectrum. Sr$_{3-x}$Si$_2$O$_4$N$_2$:xEu^{2+} shows a typical emission band peaking at $\sim$600 nm under 460 nm excitation, which perfectly matches the emission of blue InGaN light-emitting diodes. For Ce^{3+}/Li$^+$-codoped Sr$_3$Si$_2$O$_4$N$_2$, one excitation band is in the UV range (280−350 nm) and the other in the UV blue range (380−420 nm), which matches emission of near-UV light-emitting diodes. Emission of Sr$_{3-2x}$Si$_2$O$_4$N$_2$:xCe^{3+},xLi$^+$ shows a asymmetric broad band peaking at $\sim$520 nm. The long-wavelength excitation and emission of Eu^{2+} and Ce^{3+}/Li$^+$-doped Sr$_3$Si$_2$O$_4$N$_2$ make them attractive for applications in phosphor-converted white light-emitting diodes.
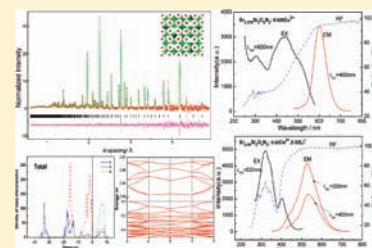
■ INTRODUCTION

During the past decade, (oxo)nitridosilicates and (oxo)-nitridoaluminosilicates have demonstrated remarkable potential capacity as host materials for phosphors used in phosphor-converted light-emitting diodes (pc-LEDs) due to their outstanding thermal and chemical stability, excellent luminescence properties, and structural diversity.[1−4] A certain number of these compounds have been synthesized as hosts for rare-earth-doped phosphors, such as α/β-SiAlONs:Eu^{2+}/Ce^{3+},[5−11] CaAlN$_3$:Eu^{2+}/Ce^{3+},[12,13] and M$_3$Si$_6$O$_{12}$N$_2$:Eu^{2+} (M = Sr, Ba)[14] and MSiN$_2$:Eu^{2+}/Ce^{3+},[15−17] M$_2$Si$_5$N$_8$:Eu^{2+}/Ce^{3+},[18−22] and MSi$_2$O$_2$N$_2$:Eu^{2+}/Ce^{3+}[23−28] (M = Ca, Sr, Ba). All of these phosphors can be efficiently excited by near-UV or blue light and emit visible light, especially the red light urgently required in white pc-LEDs.

The (oxo)nitridosilicate phosphors behave superior to oxosilicate phosphors in generating red light, which is ascribed to the stronger splitting of 5d orbitals and larger nephelauxetic effect on rare-earth ions caused by the higher effective charges of nitrogen ions (N$^{3−}$) and lower electronegativity of nitrogen.[29] On the other hand, owing to the presence of N atoms, the structural networks of nitridosilicate show more complex and flexible manners. Unlike the oxygen bridge in oxosilicates that only links two [SiO$_4$] tetrahedra, the nitrogen bridge in nitridosilicates may connect three or even four neighboring [SiN$_4$] tetrahedra. Thus, the Si:N ratio varies within a broad range of 1:4−3:4 in nitridosilicates, while in oxosilicates the Si:O ratio only changes within 1:4−1:2.[30,31] As an intermediate family of compounds between oxosilicates and nitridosilicates, oxonitridosilicates also exhibit various structural diversity and excellent luminescence properties. However, compared with the large amount of oxosilicates, fewer types of nitridosilicates and oxonitridosilicates have been synthesized due to their high sensitivity to oxygen or moisture during the preparation process.

Oxonitridosilicates $MSi_2O_2N_2$ (M = Ca, Sr, Ba) have been studied for many years. Recently, another series of oxonitridosilicates $M_3Si_2O_4N_2$ (M = Ca, Sr, Ba)[32,33] has also been receiving much attention for their excellent luminescence properties, but their structural information is still not clear. More recently, $Ca_3Si_2O_4N_2$ has been reported as a cubic structure with cell parameter $a = 15.0739(2)$ Å in space group $Pa\bar{3}$, and the phosphors based on this host are promising for application in the pc-LEDs owing to its long excitation/emission wavelength and relatively moderate synthesis conditions.[34−36] In this paper, we report the synthesis and crystal and electronic structures of the oxonitridosilicate $Sr_3Si_2O_4N_2$ as well as its luminescence properties activated by Eu^{2+} and Ce^{3+}/Li^+.

■ EXPERIMENTAL SECTION

Sample Preparation. The compound $Sr_3Si_2O_4N_2$ was prepared by solid state reactions in a horizontal tube furnace using starting materials $SrCO_3$ (AR), α-Si_3N_4 (Alfa 99.9%), and SiO_2 (AR). EuF_3 (99.9%) and $CeCl_3$ (AR) were added as activators, and LiF (AR) was introduced as a charge compensator for Ce^{3+} doping. Raw materials were mixed in an agate mortar and then filled into tungsten crucibles. The operation was conducted in a glovebox with an argon atmosphere (Mikrouna, O_2 < 1 ppm, H_2O < 1 ppm). The powder mixture was preheated at 1100 °C for 2 h, fired at 1550 °C (with a heating rate 5 °C/min) for 8 h, followed by cooling down to 900 °C at a rate 5 °C/min and down to room temperature spontaneously in the furnace with power switching off. In order to prevent samples from being oxidized, all heating and cooling processes were conducted in a reductive atmosphere of 6:94 (volume) H_2/N_2. The host sample was obtained as a white powder, and the body colors for the Eu^{2+}- and Ce^{3+}-doped samples were orange and light yellow, respectively.

Characterization. X-ray diffraction (XRD) data of samples were collected on a Bruker AXS D8 Advance powder diffractometer with Cu Kα radiation (40 kV × 40 mA). Data collection was carried out over 2θ range 5−120° with 0.02°/step and a counting time of 40 s/step. Rietveld refinements on X-ray diffraction data were performed using the software TOPAS.[37]

Time-of-flight (TOF) neutron powder diffraction (NPD) was performed at the High-Pressure Preferred Orientation (HIPPO) beamline of the Manuel Lujan, Jr. Neutron Scattering Center, Los Alamos National Laboratory. For data collection, a powder sample was filled in a vanadium can that was 0.95 cm in diameter. Data collection was carried out at room temperature for 2 h with five detector banks of 40°, 60°, 90°, 120°, and 144° used simultaneously. Rietveld refinements on the NPD data were carried out using the program GSAS,[38,39] in which the backscattering data with the highest resolution from the $2\theta = 144°$ detector was used over a TOF range 3−24 ms (corresponding to 0.6−4.9 Å in d spacing).

Density functional theory (DFT) calculation for $Sr_3Si_2O_4N_2$ was performed with the Cambridge Serial Total Energy Package (CASTEP) code,[40] in which a plane wave basis set was chosen for expansion of valence−electron wave functions at the local density approximation (LDA) level. There are two steps of calculations to obtain the electronic band structure of $Sr_3Si_2O_4N_2$. The first step was to optimize its crystal structure using the Broyden−Fletcher−Goldfarb−Shannon (BFGS) method,[41] for which the crystallographic data refined from the XRD data were used as initial values. The second step was to calculate the band structure and density of states (DOS). For the calculations, the energy cutoff of the plane wave basis set was selected as 340 eV and K-point sampling was chosen as the 2 × 2 × 2 Monkhorst-Pack grid (separation ≈ 0.04 Å^{-1}). Criterion for the self-consistent field (SCF) was eigenenergy convergence within 1.0×10^{-7} eV/atom. The pseudopotential of each atom was constructed from the CASTEP database.

To confirm the element compositions of the sample, the nitrogen content was analyzed by using an elemental analyzer (Vario EL, Germany). Measurement was conducted in an O_2 atmosphere, and the sample was heated to 1200 °C with a heating rate of 5 °C/min. The nitrogen content (weight %) obtained from the host sample was ~6.85%, in accordance with that in the formula $Sr_3Si_2O_4N_2$ (6.82%). The molar ratio of Sr:Si was analyzed to be ~1.6 (versus nominal 1.5) by inductively coupled plasma-atomic emission spectrometry (ICP-AES, PROFILE SPEC Leeman, USA). All of these confirmed the formula $Sr_3Si_2O_4N_2$.

The diffuse reflection spectrum was recorded by a UV-3100 UV−vis−-NIR spectrometer (Shimadzu, Japan) using the white powder $BaSO_4$ as a reference. Photoluminescence emission and excitation spectra were measured at room temperature using a Hitachi F4500 fluorescent spectrophotometer (Japan) with a 150 W Xe lamp as the excitation source. Spectrum correction was applied, and color coordinates were calculated using the spectra data.

■ RESULTS AND DISCUSSION

Crystal Structure. $Sr_3Si_2O_4N_2$ crystallizes in a cubic cell, and the powder XRD pattern was indexed with the unit cell parameter $a = 15.6593(1)$ Å with space group $Pa\bar{3}$ (No. 205), Z = 24. The crystal structure of $Sr_3Si_2O_4N_2$ was analyzed on the basis of the XRD data with the $Ba_3Ga_2O_6$ structure as a starting model.[42] However, an inevitable problem arises from N/O distribution analysis. X-ray diffraction is not able to effectively distinguish the O and N because of their similar X-ray scattering factors. Fortunately, owing to the significant difference between the neutron scattering lengths of oxygen and nitrogen [$b(O) = 5.803 \times 10^{-15}$ m, $b(N) = 9.36 \times 10^{-15}$ m],[43] it is feasible to distinguish O and N by neutron diffraction data. In this work, Rietveld refinement using TOF-NPD data of $Sr_3Si_2O_4N_2$ was performed and the distribution of O and N atoms in $Sr_3Si_2O_4N_2$ clearly determined. The observed and calculated X-ray and TOF neutron powder diffraction patterns for $SrSi_2O_4N_2$ as well as difference profile of the Rietveld refinement are illustrated in Figures 1 and 2, respectively. The
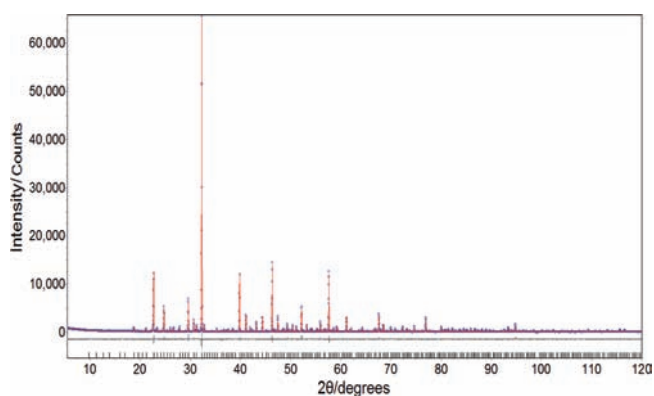
Figure 1. Observed (blue dots) and calculated (red line) powder XRD patterns as well as difference profile (gray line) for Rietveld structure analysis of $Sr_3Si_2O_4N_2$.

results of structure refinements based on X-ray and TOF-neutron powder diffraction data are summarized in Table 1. The atomic coordinates, equivalent displacement parameters, and site occupancy factors obtained from TOF-NPD data are listed in Table 2. All refined crystallographic parameters well satisfy the reflection conditions, and good fits are obtained with $R_p = 6.54$, $R_{wp} = 9.93$, GOF = 1.75 (XRD data) and $R_p = 0.85$, $R_{wp} = 2.03$, GOF = 1.18 (TOF-NPD data).

It is worth noticing that $Sr_3Si_2O_4N_2$ is not exactly isostructural with $Ca_3Si_2O_4N_2$. Both $Ca_3Si_2O_4N_2$ and $Sr_3Si_2O_4N_2$ have the same space group and similar 12-ring
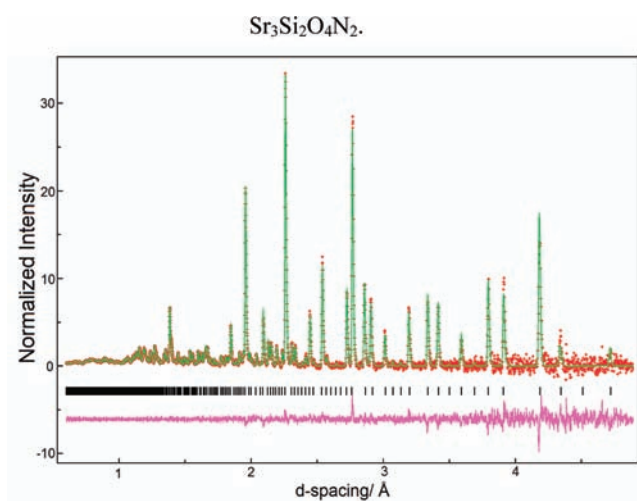
Figure 2. Observed (red crosses) and calculated (green line) TOF-NPD patterns as well as difference profile (purple line) for Rietveld structure analysis of $Sr_3Si_2O_4N_2$.

Table 1. Crystallographic Data of $Sr_3Si_2O_4N_2$ Derived from Rietveld Refinement of X-ray Diffraction and TOF-Neutron Powder Diffraction Data

formula	$Sr_3Si_2O_4N_2$	$Sr_3Si_2O_4N_2$
cryst syst/space group	cubic/$Pa\overline{3}$ (No. 205)	cubic/$Pa\overline{3}$ (No. 205)
radiation	X-ray	TOF-neutron
lattice parameter a (Å)	15.6593(1)	15.6220(9)
cell vol. (Å³)	3839.87(9)	3812.56(9)
formula units per cell, Z	24	24
structure refinement	Topas	GSAS
temp. (K)	293	293
profile range	$5 \leq 2\theta \leq 120$	$0.6 \leq d \leq 4.8$
no. of data points	5824	5341
profile function	PV_TCHZ	Gaussian
R_p	6.54	0.85
R_{wp}	9.93	2.03
R_{exp}	5.68	1.72
GOF	1.75	1.18

$Sr_3Si_2O_4N_2$ shows a similar ring structure to accommodate six distinctly crystallographic Sr^{2+} sites (five fully occupied and one-half occupied), which is isostructural to $Ba_3Ga_2O_6$.[42]

The building unit in $Sr_3Si_2O_4N_2$ is 12 ring that consists of 12 $[SiO_2N_2]$ tetrahedra, which connect each other by sharing N atoms at bridging positions with a Q^2 link type.[44] While in the 12 ring, O atoms locate at terminal positions. A similar structure built by 12 rings also appears in the nitridosilicates $M_7Si_6N_{15}$ (M = La, Ce, Pr).[45] Most previously reported oxonitridosilicates are a layered framework, such as $M_3Si_6O_{12}N_2$[14] and $MSi_2O_2N_2$ (M = Ca, Sr, Ba).[25,26,31] The layers consist of vertex-shared $[SiO_3N]$ and $[SiON_3]$ tetrahedra with Q^3 type. Figure 3 illustrates the building unit (12 ring) in $Sr_3Si_2O_4N_2$ viewed from different directions. When viewed
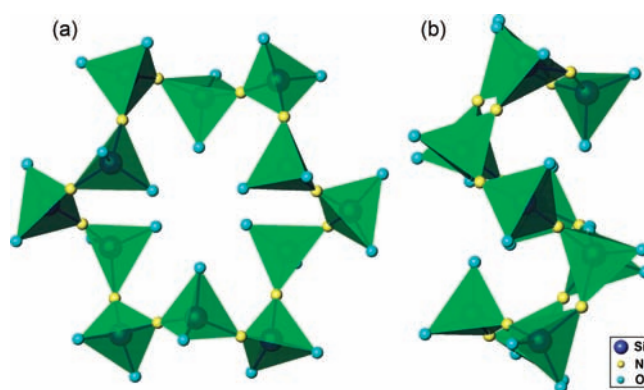
Figure 3. Corrugated 12-ring structural view in the [111] direction (a) and [110] direction (b).

along the [111] direction the ring looks like a highly symmetric hexagon, while when viewed along the [110] direction the ring is corrugated as the "S" shape. The relationship between the 12 rings and the unit cell is represented in Figure 4. The structure of $Sr_3Si_2O_4N_2$ along [001] is represented in Figure 4a. For a clear representation, the simplified Si−N rings (Sr^{2+} and $O^{2−}$ ions are omitted) are depicted in Figure 4b, in which the rings are piled in the $Sr_3Si_2O_4N_2$ unit cell disconnectedly on different directions.

The 12 rings are linked by six distinct crystallographic Sr^{2+} sites, among which the sites from Sr1 to Sr5 are distributed at the interstitial positions between the adjacent rings and the sites
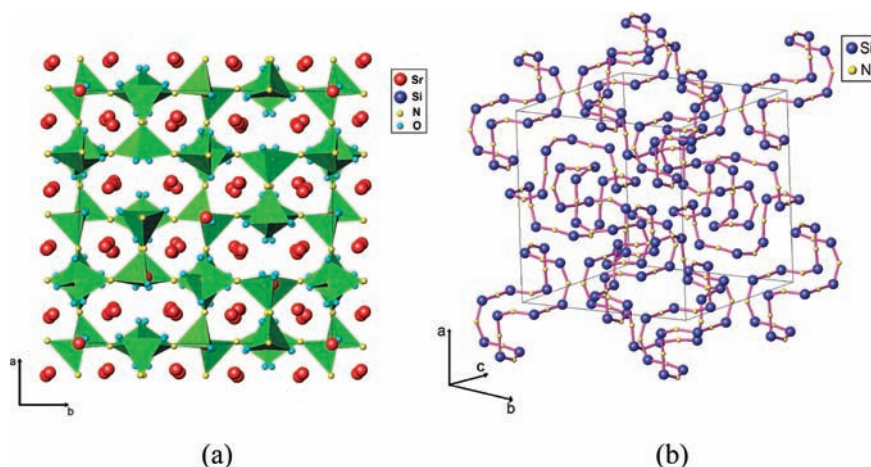
framework, but the crystallographic sites of Ca^{2+} and Sr^{2+} were different. $Ca_3Si_2O_4N_2$ has seven distinct crystallographic Ca^{2+} sites, and three of them are not fully occupied.[34,35] However,

Table 2. Atomic Coordinates, Equivalent Displacement Parameters, and Site Occupancy Factors for $Sr_3Si_2O_4N_2$ Determined by Rietveld Refinement on TOF-NPD Data

atom	multiplicity	x	y	z	s.o.f.	$U_{eq}/Å^2$
Sr1	4a	0	0	0	1	0.0095(2)
Sr2	8c	0.2368(5)	0.2368(5)	0.2368(5)	0.5	0.0473(6)
Sr3	8c	0.3721(0)	0.3721(0)	0.3721(0)	1	0.0089(4)
Sr4	8c	0.1365(6)	0.1365(6)	0.1365(6)	1	0.0234(1)
Sr5	24d	0.3585(5)	0.1371(9)	0.3711(3)	1	0.0158(7)
Sr6	24d	0.1152(9)	0.1025(5)	0.3838(8)	1	0.0100(9)
Si1	24d	0.5012(2)	0.2291(0)	0.2337(0)	1	0.0088(7)
Si2	24d	0.4809(0)	0.0220(3)	0.2559(7)	1	0.0039(9)
O1	24d	0.2642(8)	0.2687(9)	0.4102(8)	1	0.0170(3)
O2	24d	0.3346(8)	0.4834(5)	0.4801(2)	1	0.0179(5)
O3	24d	0.0884(5)	0.2769(2)	0.2236(1)	1	0.0163(3)
O4	24d	0.0198(2)	0.9730(9)	0.1588(7)	1	0.0199(5)
N1	24d	0.1244(2)	0.2556(3)	0.5094(5)	1	0.0166(8)
N2	24d	0.2495(5)	0.1247(7)	0.5033(2)	1	0.0153(3)

3542

dx.doi.org/10.1021/ic202340q | Inorg. Chem. 2012, 51, 3540−3547

Figure 4. Structure of $Sr_3Si_2O_4N_2$ viewed along [001] (a); simplified Si−N rings (b).

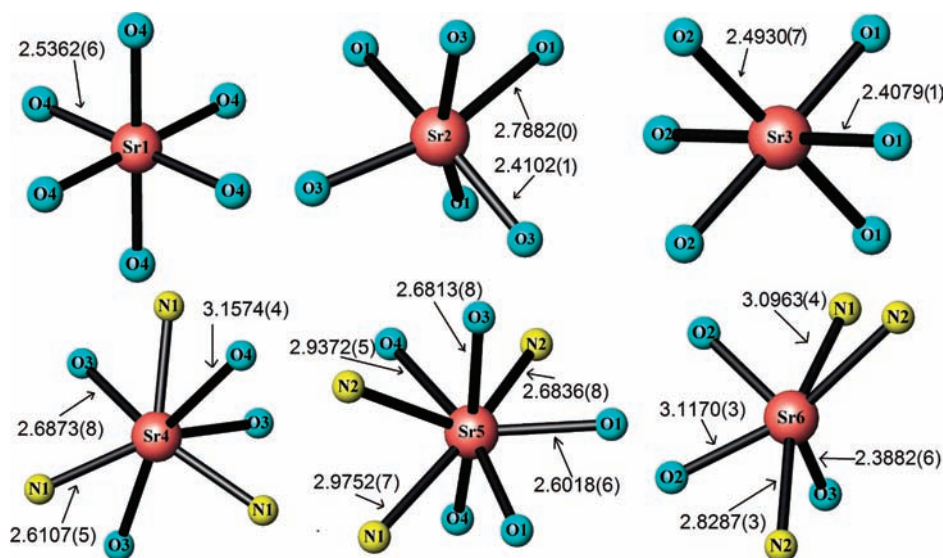**Figure 5.** Coordination spheres and bond lengths (Å) of the six different Sr^{2+} sites in $Sr_3Si_2O_4N_2$.

Sr6 located inside the rings. The coordination spheres and bond lengths of Sr−O and Sr−N for the six different Sr^{2+} sites are depicted in Figure 5. The refinement results of Sr^{2+} site occupancies indicate that one of the Sr sites (Sr2) is only one-half occupied, accompanied with a large equivalent displacement parameter. This one-half occupied site is also found in the structure of $Ba_3Ga_2O_6$. As shown in Table 3, the bond lengths of Sr−O and Sr−N are in the range of 2.39−3.16 and 2.61−3.10 Å, respectively, while the valence bond sum of Sr^{2+} is in the range of 1.7−2.4. The bond lengths of Si−N and Si−O in $[SiO_2N_2]$ tetrahedra are in the typical ranges of 1.66−1.73 and 1.62−1.66 Å, respectively, and the valence bond sums of two Si^{4+} are 3.9 and 4.1, respectively. The bond lengths of Si−O are slightly shorter than that of the Si−N bonds as expected. Apparently, Si−O and Si−N bond in $Sr_3Si_2O_4N_2$ are in the normal range observed in other oxonitridosilicates ($CaSi_2O_2N_2$: Si−O = 1.59−1.62 Å and Si−N = 1.68−1.78 Å).[31] The angle values of the (O/N)−Si−(O/N) in the tetrahedra ranging from 102° to 116° are also close to the ideal value of 109°, and the Si−N−Si angles between the $[SiO_2N_2]$ tetrahedra vary within 157−169°.

Band Structure. The band structure of $Sr_3Si_2O_4N_2$ was calculated using density functional theory (DFT) methods,[46]

which shows an indirect band gap (E_g = 2.84 eV) in Figure 6. Figure 7 shows the total and partial density of states (DOS) of $Sr_3Si_2O_4N_2$. The conduction band is mainly composed by Sr 3d orbitals, while the valence band is mainly composed by N 2p

Table 3. Selected Bond Lengths and Angles of $Sr_3Si_2O_4N_2$ Based on TOF-NPD Data

bond	length (Å)	bond	length (Å)
Sr1−O4	2.5362(6)	Sr2−O1	2.7882(0)
Sr3−O1	2.4079(1)	Sr4−N1	2.6107(5)
Sr4−O4	3.1574(4)	Sr5−O1	2.6018(6)
Sr5−N1	2.9752(7)	Sr5−N2	2.6836(8)
Sr6−O2	3.1170(3)	Sr6−N1	3.0963(4)
Sr6−N2	2.8287(3)	Sr6−O3	2.3882(6)
Si1−O1	1.6188(5)	Si2−O2	1.6565(7)
Si1−N2	1.7317(7)	Si2−N1	1.6604(4)
bond	angle (deg)	bond	angle (deg)
O2−Si2−N2	102.15(9)	O1−Si1−N1	109.22(4)
N1−Si2−N2	115.55(6)	N1−Si1−N2	112.30(0)
O2−Si2−O4	112.4679	O1−Si1−O3	115.06(4)
Si1−N2−Si2	168.57(6)	Si1−N1−Si2	156.93(9)
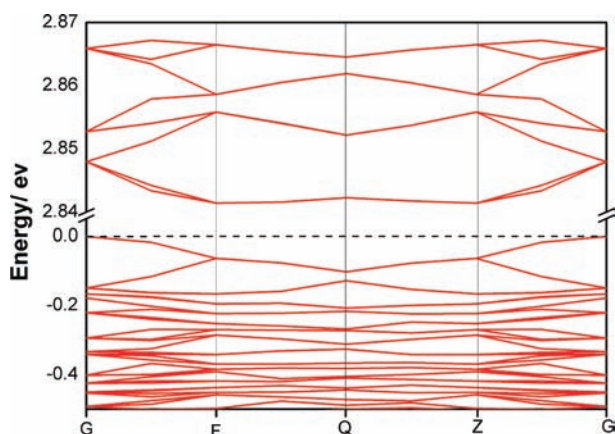
Figure 6. Band structure of $Sr_3Si_2O_4N_2$.

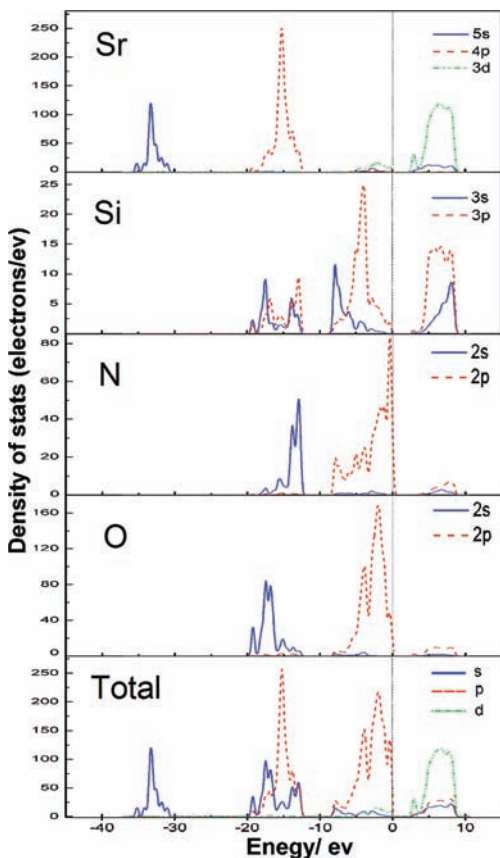**Figure 7.** Total and partial density of states of $Sr_3Si_2O_4N_2$.

and O 2p orbitals. The N 2p orbitals have more contributions than the O 2p orbitals to the top of the valence band; thus, it is deduced that nitrogen benefits reduction of the band gap for $Sr_3Si_2O_4N_2$.

Diffuse Reflection Spectra. The diffuse reflection spectra of undoped and Eu^{2+}- and Ce^{3+}/Li^+-doped $Sr_3Si_2O_4N_2$ are shown in Figure 8. $Sr_3Si_2O_4N_2$ shows a high reflection in the visible range and a remarkable drop around 280 nm that corresponds to the band transition in the $Sr_3Si_2O_4N_2$ host lattice, which leads to its white body color. The Eu^{2+}-doped $Sr_3Si_2O_4N_2$ shows a wide absorption range in the UV to 500 nm, and the Ce^{3+}/Li^+-doped phosphor shows absorption in the wavelength range in the UV to 420 nm. The intense reflection in the visible spectral range is in agreement with the observed
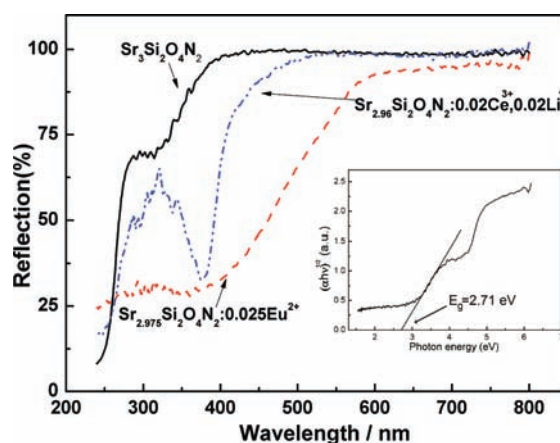

Figure 8. Diffuse reflection spectra of doped and undoped $Sr_3Si_2O_4N_2$ (Inset) Relationship between the absorption coefficient and the photon energy for $Sr_3Si_2O_4N_2$.

orange and light yellow body color for Eu^{2+}- and Ce^{3+}/Li^+-doped materials, respectively. The band gap is estimated according to eq 1.

$$(\alpha h\upsilon)^n = A(h\upsilon - E_g) \tag{1}$$

where $h\upsilon$ is the incident photon energy, A is a constant, α is the absorption coefficient, and $n = 2$ for a direct transition or $1/2$ for an indirect transition.[47,48] The values of $(\alpha h\upsilon)^{1/2}$ are plotted as a function of the incident photon energy $(h\upsilon)$ as illustrated in the inset of Figure 8. From the linear extrapolation of $(\alpha h\upsilon)^{1/2} = 0$, the E_g value was estimated to be about 2.71 eV, which is consistent with the value of 2.84 eV obtained from DFT calculation.

Luminescence Properties of Eu^{2+}- and Ce^{3+}-Doped $Sr_3Si_2O_4N_2$. $Sr_3Si_2O_4N_2$:Eu^{2+} powder has orange body color due to the $4f^7 \rightarrow 4f^65d^1$ absorption of Eu^{2+} in the blue spectral range. The excitation, emission, and diffuse reflection spectra of phosphor $Sr_{2.975}Si_2O_4N_2$:$0.025Eu^{2+}$ are shown in Figure 9. $Sr_3Si_2O_4N_2$:Eu^{2+} can be efficiently excited by blue light (400–500 nm), which is very advantageous for application in the pc-LEDs combined with highly efficient blue-InGaN chips. Subsequently, a typical broad-band red emission with a maximum at ∼600 nm is obtained (fwhm ≈ 80 nm). Compared with another oxonitridosilicate phosphor $SrSi_2O_2N_2$:Eu^{2+}
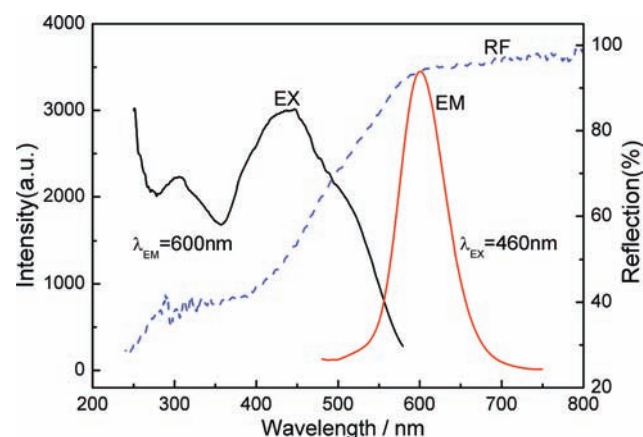

Figure 9. Excitation, emission (solid lines), and diffuse reflection (dash lines) spectra of $Sr_{2.975}Si_2O_4N_2$:$0.025Eu^{2+}$.

3544

dx.doi.org/10.1021/ic202340q | *Inorg. Chem.* 2012, 51, 3540−3547

peaking at 560 nm,[28] $Sr_3Si_2O_4N_2$:Eu^{2+} bears a lower N content but shows a larger red shift. These could be attributed to the different Sr^{2+} coordination environments in these two compounds. In the layer structure $SrSi_2O_2N_2$, Sr^{2+} ions locate between the $[Si_2O_2N_2]^{2-}$ layers and coordinate only with O atoms instead of bridging N atoms inside $[Si_2O_2N_2]^{2-}$ layers. However, in $Sr_3Si_2O_4N_2$, the six types of Sr^{2+} ions distribute both inside and outside the corrugated 12 rings, which allows Sr^{2+} ions to directly conjugate with N atoms (Sr4, Sr5, and Sr6 are coordinated by O atoms and N atoms, see Figure 5). Considering the red emission of Eu^{2+}-doped oxonitridosilicate $Sr_3Si_2O_4N_2$, the contribution of N atoms in this large red shift cannot be ignored. These Sr^{2+} ions (Sr4, Sr5, and Sr6) coordinated with N atoms are probably the preferential lattice sites for Eu^{2+} to replace. This structural feature is consistent with the band structure, in which N atoms show a very important contribution to the valence band. With higher effective charges of N^{3-} and lower electronegativity of N, nitrogen coordination causes stronger splitting of 5d orbitals and a larger nephelauxetic effect; remarkable red shifts in both excitation and emission spectra are expected.

The influence of the Eu^{2+} concentration on the luminescence properties was also investigated. Figure 10 shows the emission spectra of $Sr_{3-x}Si_2O_4N_2$:xEu^{2+} phosphors with various Eu^{2+} concentrations ($x = 0.003-0.06$). With Eu^{2+} concentration
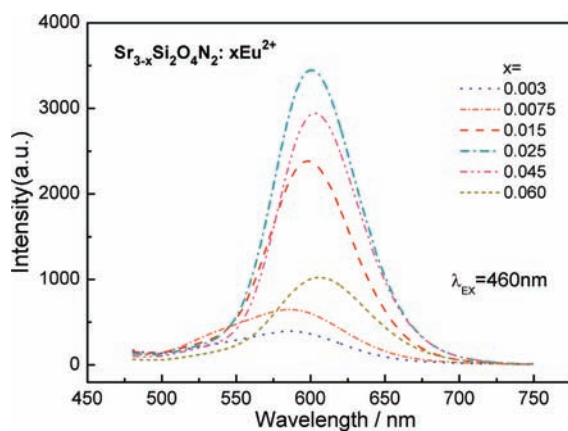
Figure 10. Emission spectra of $Sr_{3-x}Si_2O_4N_2$:xEu^{2+} with varied Eu^{2+} concentrations under an excitation of 460 nm. The weak emission at around 530 nm at the low concentration range of Eu^{2+} from $x = 0.03$ to 0.0075 is due to the minor second phase of the oxonitridosilicates.

increase, the luminescence intensity increases and reaches a maximum at $x \approx 0.025$. When the Eu^{2+} concentration exceeds 0.025, concentration quenching occurs. The emission peak position of the $Sr_{3-x}Si_2O_4N_2$:xEu^{2+} phosphors also shift from 585 to 606 nm as Eu^{2+} concentration increase, which is attribute to the reabsorption of Eu^{2+}. The increase of Eu^{2+} concentration raises the energy transfer probability between Eu^{2+} ions, which reduces the high-energy portion in the whole emission profile, and then the lowered overall energy is represented by the red shift. In summary, $Sr_3Si_2O_4N_2$:Eu^{2+} phosphor is a good red phosphor candidate for creating warm white light when combined with a blue LED and a green (or yellow) phosphor.

The excitation, emission, and diffuse reflection spectra of $Sr_{2.96}Si_2O_4N_2$:$0.02Ce^{3+}$,$0.02Li^+$ are depicted in Figure 11. The emission spectrum shows a broad band with a maximum at 520 nm (fwhm ≈ 120 nm). As we know, the emission of Ce^{3+} can
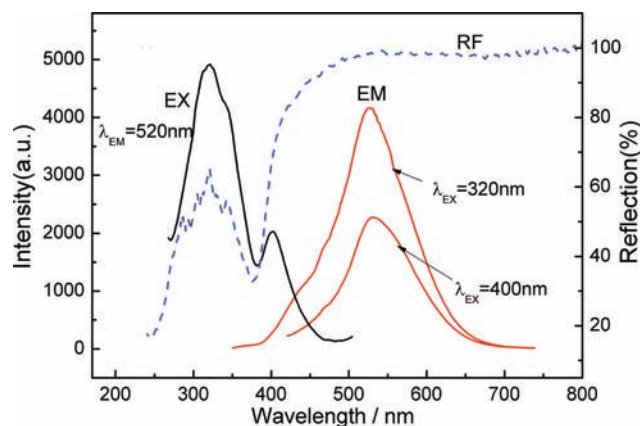
Figure 11. Excitation, emission (solid lines), and diffuse reflection (dash lines) spectra of $Sr_{2.96}Si_2O_4N_2$:$0.02Ce^{3+}$,$0.02Li^+$.

be attributed to the transition from the 5d band to the doublet 4f ground level ($^2F_{5/2}$ and $^2F_{7/2}$); thus, the typical Ce^{3+} emission normally is a shouldered band. However, in $Sr_3Si_2O_4N_2$ host, there are six Sr^{2+} sites that could be replaced by Ce^{3+} (maybe some sites are preferential); thus, the multisites of Ce^{3+} make the emission band asymmetric. The excitation spectrum displays two principle bands: one in the UV range (280−350 nm) and another in the UV blue range (380−420 nm). The emission and excitation intensities of the former are much stronger than that of the latter. Figure 12 shows the influence of the Ce^{3+} concentration ($x = 0.005-0.05$) on the emission intensity of $Sr_{3-2x}Si_2O_4N_2$:xCe^{3+},xLi^+. With an increase of Ce^{3+}
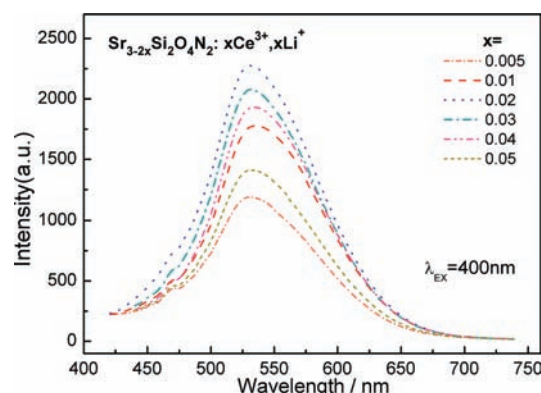
Figure 12. Emission spectra of $Sr_{3-2x}Si_2O_4N_2$:xCe^{3+},xLi^+ with varied Ce^{3+} and Li^+ concentrations under an excitation of 400 nm.

concentration, the luminescence intensity becomes higher and arrives at a maximum at $x = 0.02$. Different from Eu^{2+}-doped $Sr_3Si_2O_4N_2$ phosphors, the shift of the emission peak position herein is not notable with a Ce^{3+} concentration increase. To understand this difference better, further research is necessary. However, compared with $SrSi_2O_2N_2$:Ce^{3+} that exhibits an emission band centered at 470 nm,[24] $Sr_3Si_2O_4N_2$:Ce^{3+} also shows a larger red shift in both excitation and emission spectra. With an intense absorption and excitation band in the UV blue wavelength region (300−420 nm), $Sr_{3-2x}Si_2O_4N_2$:xCe^{3+},xLi^+ would be a novel yellow phosphor for pc-LEDs combined with near-UV chips.

Figure 13 shows the chromaticity coordinates of the $Sr_3Si_2O_4N_2$ phosphors doped with Eu^{2+} and Ce^{3+}/Li^+ on the Commission Internationale del'Eclairage (CIE) chromaticity

diagram. The phosphor $Sr_{2.975}Si_2O_4N_2:0.025Eu^{2+}$ has chromaticity coordinates (0.570, 0.423), while the phosphor
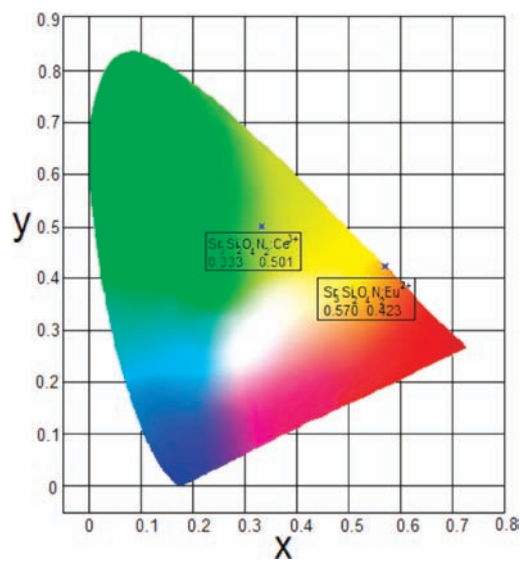
Figure 13. Chromaticity coordinates of $Sr_{2.975}Si_2O_4N_2:0.025Eu^{2+}$ and $Sr_{2.96}Si_2O_4N_2:0.02Ce^{3+},0.02Li^+$ phosphors under 460 and 400 nm excitation, respectively (represented on the CIE chromaticity diagram).

$Sr_{2.96}Si_2O_4N_2:0.02Ce^{3+},0.02Li^+$ has chromaticity coordinates (0.333, 0.501).

CONCLUSION

The crystal structure of the oxonitridosilicate $Sr_3Si_2O_4N_2$ shows a highly corrugated 12-ring framework. The building unit consists of 12 vertex-sharing $[SiO_2N_2]$ tetrahedra with bridging N atoms and terminal O atoms (12 ring). DFT calculations reveal an indirect band gap of 2.84 eV for $Sr_3Si_2O_4N_2$, which is in good agreement with the value determined from the reflection spectra (~2.71 eV). Due to this structural feature, N atoms may directly coordinate to Sr^{2+} at some cation sites; thus, the excitation and emission bands of both Eu^{2+}- and Ce^{3+}/Li^+-doped $Sr_3Si_2O_4N_2$ phosphors show significant red shifts. Under excitation in the range 400−500 nm, $Sr_3Si_2O_4N_2:Eu^{2+}$ shows a red emission around 600 nm (fwhm ≈ 80 nm); thus, this phosphor is very attractive to be employed in pc-LEDs combined with blue chips. While $Sr_3Si_2O_4N_2:Ce^{3+},Li^+$ phosphor shows a yellow emission peak at 520 nm (fwhm ≈ 120 nm) under excitation in the range 300−400 nm, it may also perform as an attractive candidate phosphor for pc-LEDs combined with near-UV chips.

ASSOCIATED CONTENT

Ⓢ Supporting Information

TOF-neutron crystallographic file for $Sr_3Si_2O_4N_2$ (CIF). This material is available free of charge via the Internet at http://pubs.acs.org.

AUTHOR INFORMATION

Corresponding Author

*Phone: +86-010-62754188. E-mail: xpjing@pku.edu.cn.

Notes

The authors declare no competing financial interest.

ACKNOWLEDGMENTS

REFERENCES

(1) Zeuner, M.; Pagano, S.; Schnick, W. *Angew. Chem., Int. Ed.* **2011**, *50*, 7754−7775.
(2) Schnick, W. *Phys. Status Solidi, Rapid Res. Lett.* **2009**, *3*, A113−A114.
(3) Höppe, H. A. *Angew. Chem., Int. Ed.* **2009**, *48*, 3572−3582.
(4) Xie, R. J.; Hirosaki, N.; Mitomo, M. *J. Electroceram.* **2008**, *21*, 370−373.
(5) Liu, L. H.; Xie, R. J.; Hirosaki, N.; Takeda, T.; Li, J. G.; Sun, X. D. *J. Am. Ceram. Soc.* **2009**, *92*, 2668−2673.
(6) Suehiro, T.; Hirosaki, N.; Xie, R. J.; Sakuma, K.; Mitomo, M.; Ibukiyama, M.; Yamada, S. *Appl. Phys. Lett.* **2008**, *92*, 191904.
(7) Li, H. L.; Xie, R. J.; Hirosaki, N.; Suehiro, T.; Yajima, Y. *J. Electrochem. Soc.* **2008**, *155*, J175−J179.
(8) Li, H. L.; Hirosaki, N.; Xie, R. J.; Suehiro, T.; Mitomo, M. *Sci. Technol. Adv. Mater.* **2007**, *8*, 601−606.
(9) Xie, R. J.; Hirosaki, N.; Mitomo, M.; Suehiro, T.; Xu, X.; Tanaka, H. *J. Am. Ceram. Soc.* **2005**, *88*, 2883−2888.
(10) Xie, R. J.; Hirosaki, N.; Sakuma, K.; Yamamoto, Y.; Mitomo, M. *Appl. Phys. Lett.* **2004**, *84*, 5404−5406.
(11) Shioi, K.; Hirosaki, N.; Xie, R. J.; Takeda, T.; Li, Y. Q.; Matsushita, Y. *J. Am. Ceram. Soc.* **2010**, *93*, 465−469.
(12) Li, J. W.; Watanabe, T.; Sakamoto, N.; Wada, H. S.; Setoyama, T.; Yoshimura, M. *Chem. Mater.* **2008**, *20*, 2095−2105.
(13) Li, Y. Q.; Hirosaki, N.; Xie, R. J.; Takeda, T.; Mitomo, M. *Chem. Mater.* **2008**, *20*, 6704−6714.
(14) Braun, C.; Seibald, M.; Borger, S. L.; Oeckler, O.; Boyko, T. D.; Moewes, A.; Miehe, G.; Tucks, A.; Schnick, W. *Chem.—Eur. J.* **2010**, *16*, 9646−9657.
(15) Duan, C. J.; Wang, X. J.; Otten, W. M.; Delsing, A. C. A.; Zhao, J. T.; Hintzen, H. T. *Chem. Mater.* **2008**, *20*, 1597−1605.
(16) Gal, Z. A.; Mallinson, P. M.; Orchard, H. J.; Clarke, S. J. *Inorg. Chem.* **2004**, *43*, 3998−4006.
(17) Le Toquin, R.; Cheetham, A. K. *Chem. Phys. Lett.* **2006**, *423*, 352−356.
(18) Li, H. L.; Xie, R. J.; Hirosaki, N.; Takeda, T.; Zhou, G. H. *Int. J. Appl. Ceram. Technol.* **2009**, *6*, 459−464.
(19) Xie, R. J.; Hirosaki, N.; Suehiro, T.; Xu, F. F.; Mitomo, M. *Chem. Mater.* **2006**, *18*, 5578−5583.
(20) Li, Y. Q.; van Steen, J. E. J.; van Krevel, J. W. H.; Botty, G.; Delsing, A. C. A.; DiSalvo, F. J.; de With, G.; Hintzen, H. T. *J. Alloys Compd.* **2006**, *417*, 273−279.
(21) Li, Y. Q.; de With, G.; Hintzen, H. T. *J. Lumin.* **2006**, *116*, 107−116.
(22) Hoppe, H. A.; Lutz, H.; Morys, P.; Schnick, W.; Seilmeier, A. *J. Phys. Chem. Solids* **2000**, *61*, 2001−2006.
(23) Bachmann, V.; Justel, T.; Meijerink, A.; Ronda, C.; Schmidt, P. J. *J. Lumin.* **2006**, *121*, 441−449.
(24) Li, Y. Q.; de With, G.; Hintzen, H. T. *J. Mater. Chem.* **2005**, *15*, 4492−4496.
(25) Kechele, J. A.; Oeckler, O.; Stadler, F.; Schnick, W. *Solid State Sci.* **2009**, *11*, 537−543.
(26) Oeckler, O.; Stadler, F.; Rosenthal, T.; Schnick, W. *Solid State Sci.* **2007**, *9*, 205−212.
(27) Bachmann, V.; Ronda, C.; Oeckler, O.; Schnick, W.; Meijerink, A. *Chem. Mater.* **2009**, *21*, 316−325.
(28) Li, Y. Q.; Delsing, A. C. A.; de With, G.; Hintzen, H. T. *Chem. Mater.* **2005**, *17*, 3242−3248.
(29) Xie, R. J.; Hirosaki, N.; Sakuma, K.; Kimura, N. *J. Phys. D: Appl. Phys.* **2008**, *41*, 144013.

(30) Schnick, W.; Schlieper, T.; Huppertz, H.; Kollisch, K.; Orth, M.; Bettenhausen, R.; Schwarze, B.; Lauterbach, R. *Phosphorus Sulfur* **1997**, *125*, 163−172.

(31) Höppe, H. A.; Stadler, F.; Oeckler, O.; Schnick, W. *Angew. Chem., Int. Ed.* **2004**, *43*, 5540−5542.

(32) Tim, F.; Wolfram, H.; Frank, J. U.S. Patent 7791256 B2, June 21, 2007.

(33) Hirosaki, N.; Xie, R. J. U.S. Patent 7540977, June 2, 2009.

(34) Ali, S. Doctoral Thesis, Stockholm University, Stockholm, Sweden., 2009.

(35) Wang, X. M.; Wang, C. H.; Wu, M. M.; Wang, Y. X.; Jing, X. P. *J. Mater. Chem.* **2012**, *22*, 3388−3394.

(36) Chiu, Y. C.; Huang, C. H.; Lee, T. J.; Liu, W. R.; Yeh, Y. T.; Jang, S. M.; Liu, R. S. *Opt Express* **2011**, *19* (suppl 3), A331−9.

(37) *TOPAS V3.1: General Profile and Structure Analysis Software for Powder Diffraction Data*; B. A., Karlsruhe, Germany.

(38) Larson, A. C.; Von Dreele, R. B. *General Structure Analysis System (GSAS)*; Los Alamos National Laboratory Report LAUR 86-748, 2004.

(39) Toby, B. H. *J. Appl. Crystallogr.* **2001**, *34*, 210−213.

(40) Segall, M. D.; Lindan, P. J. D.; Probert, M. J.; Pickard, C. J.; Hasnip, P. J.; Clark, S. J.; Payne, M. C. *J. Phys.: Condens. Matter* **2002**, *14*, 2717−2744.

(41) Nocedal, J. *Math. Comput.* **1980**, *35*, 773−782.

(42) Kahlenberg, V. *Cryst. Res. Technol.* **2001**, *36*, 319−326.

(43) Irran, E.; Kollisch, K.; Leoni, S.; Nesper, R.; Henry, P. F.; Weller, M. T.; Schnick, W. *Chem.—Eur. J.* **2000**, *6*, 2714−2720.

(44) Lippmaa, E.; Maegi, M.; Samoson, A.; Engelhardt, G.; Grimmer, A. R. *J. Am. Chem. Soc.* **1980**, *102*, 4889−4893.

(45) Schmolke, C.; Oeckler, O.; Bichler, D.; Johrendt, D.; Schnick, W. *Chem.—Eur. J.* **2009**, *15*, 9215−9222.

(46) Gonze, X.; Beuken, J. M.; Caracas, R.; Detraux, F.; Fuchs, M.; Rignanese, G. M.; Sindic, L.; Verstraete, M.; Zerah, G.; Jollet, F.; Torrent, M.; Roy, A.; Mikami, M.; Ghosez, P.; Raty, J. Y.; Allan, D. C. *Comput. Mater. Sci.* **2002**, *25*, 478−492.

(47) Inaba, K.; Suzuki, S.; Noguchi, Y.; Miyayama, M.; Toda, K.; Sato, M. *Eur. J. Inorg. Chem.* **2008**, 5471−5475.

(48) Pankove, J. I. *Optical processes in semiconductors*; Dover Publications: 1971.

3547

dx.doi.org/10.1021/ic202340q | *Inorg. Chem.* 2012, 51, 3540−3547